Lecture Notes in Mechanical Engineering

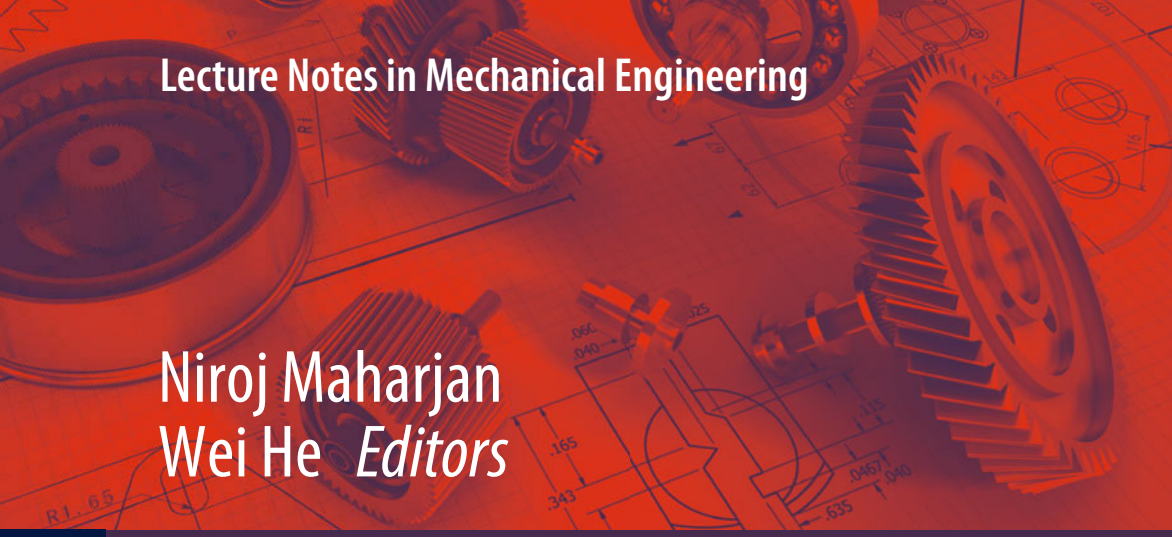

Niroj Maharjan
Wei He *Editors*

Proceedings of the 3rd International Conference on Advanced Surface Enhancement (INCASE) 2023

Surface Engineering for Sustainability

Springer

Lecture Notes in Mechanical Engineering

Lecture Notes in Mechanical Engineering (LNME) publishes the latest developments in Mechanical Engineering—quickly, informally and with high quality. Original research or contributions reported in proceedings and post-proceedings represents the core of LNME. Volumes published in LNME embrace all aspects, subfields and new challenges of mechanical engineering.

To submit a proposal or request further information, please contact the Springer Editor of your location:

Europe, USA, Africa: Leontina Di Cecco at Leontina.dicecco@springer.com
China: Ella Zhang at ella.zhang@springer.com
India: Priya Vyas at priya.vyas@springer.com
Rest of Asia, Australia, New Zealand: Swati Meherishi at swati.meherishi@springer.com

Topics in the series include:

- Engineering Design
- Machinery and Machine Elements
- Mechanical Structures and Stress Analysis
- Automotive Engineering
- Engine Technology
- Aerospace Technology and Astronautics
- Nanotechnology and Microengineering
- Control, Robotics, Mechatronics
- MEMS
- Theoretical and Applied Mechanics
- Dynamical Systems, Control
- Fluid Mechanics
- Engineering Thermodynamics, Heat and Mass Transfer
- Manufacturing Engineering and Smart Manufacturing
- Precision Engineering, Instrumentation, Measurement
- Materials Engineering
- Tribology and Surface Technology

Indexed by SCOPUS, EI Compendex, and INSPEC.

All books published in the series are evaluated by Web of Science for the Conference Proceedings Citation Index (CPCI).

To submit a proposal for a monograph, please check our Springer Tracts in Mechanical Engineering at https://link.springer.com/bookseries/11693.

Niroj Maharjan · Wei He
Editors

Proceedings of the 3rd International Conference on Advanced Surface Enhancement (INCASE) 2023

Surface Engineering for Sustainability

Springer

Editors
Niroj Maharjan
Advanced Remanufacturing
and Technology Centre (ARTC)
Singapore, Singapore

School of Engineering
Swinburne University of Technology
Hawthorn, Australia

Wei He
Singapore Institute of Manufacturing
Technology (SIMTech)
Singapore, Singapore

ISSN 2195-4356 ISSN 2195-4364 (electronic)
Lecture Notes in Mechanical Engineering
ISBN 978-981-99-8642-2 ISBN 978-981-99-8643-9 (eBook)
https://doi.org/10.1007/978-981-99-8643-9

Contents

Advanced Techniques for Surface Engineering Towards Enhanced Performance

Rotating Bending High Cycle Fatigue Property of Handheld Laser Peened A7075BE-T6511 Alloy

Kiyotaka Masaki, Yuji Sano, Yoshio Mizuta, and Satoshi Tamaki

Abstract Laser peening (LP) processing is one of surface technologies in which a metal material placed in water is irradiated with a pulse laser and peened by the generated shock wave. Since conventional laser peening requires large-scale and high-cost laser equipment, smaller and cheaper pulse laser oscillators have been desired for further industrial applications. In recent years, some handheld pulse laser oscillators have been developed by the ImPACT Program in Japan. In this study, in order to investigate the effectiveness of the new handheld laser device for LP treatment, rotating bending high cycle fatigue tests were conducted on A7075BE-T6511 aluminum alloy. As a result, the high cycle fatigue properties were significantly improved by LP treatment. The fatigue strength at 10^7 cycles is improved by about 1.5 times, and the fatigue life is extended by about 100 times than those of base metal specimens. In this study, the improvement of fatigue properties by laser peening treatment with a handheld laser oscillator was investigated from the viewpoint of peening effect and fracture mechanism.

Keywords Aluminum alloy · Handheld laser oscillator · Rotating bending high cycle fatigue · Laser Peening

K. Masaki (✉)
Saitama Institute of Technology, Fukaya 369-0293, Saitama, Japan
e-mail: masaki-k@sit.ac.jp

Y. Sano
Institute for Molecular Science, Okazaki 444-8585, Aichi, Japan
e-mail: yuji-sano@ims.ac.jp

Y. Sano · Y. Mizuta · S. Tamaki
SANKEN, Osaka University, Ibaraki 567-0047, Osaka, Japan
e-mail: y.mizuta@sanken.osaka-u.ac.jp

S. Tamaki
e-mail: tamaki@sanken.osaka-u.ac.jp

N. Maharjan and W. He (eds.), *Proceedings of the 3rd International Conference on Advanced Surface Enhancement (INCASE) 2023*, Lecture Notes in Mechanical Engineering, https://doi.org/10.1007/978-981-99-8643-9_1

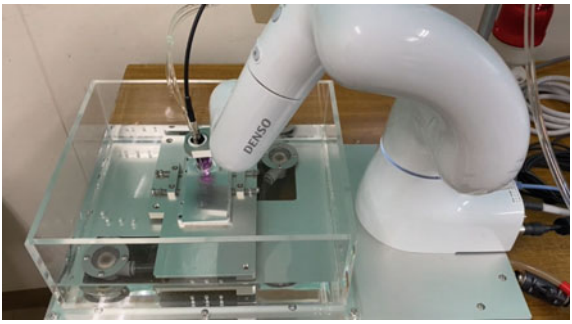

Fig. 1 The newly developed handheld pulse laser oscillator on a robot arm

1 Introduction

Laser peening (LP) processing is one of surface modification technologies. In this process, a pulse laser is irradiated to a metal material placed in water, and the metal is peened by the generated shock wave [1]. At that time, since conventional LP treatment requires large-scale and expensive pulse laser oscillator, smaller and cheaper pulse laser oscillators have been desired for industrial applications [2, 3]. Recently, new handheld pulse laser oscillators as shown in Fig. 1 have been developed by the ImPACT program in Japan [4, 5]. If it turns out that this device can be used as an LP treatment device, there is a possibility that LP treatment can be applied to various industrial fields. In this study, in order to investigate the effectiveness of the newly developed handheld pulse laser oscillator for LP treatment, rotating bending fatigue tests were conducted on Al–Zn–Mg–Cu system aluminum alloys treated by LP.

2 Experimental Methods

2.1 Material

The material used in this study is A7075BE-T6511 aluminum alloy. After extruding into a bar with a diameter of 15 mm, T6511 heat treatment was applied, namely, solution heat treatment, residual stress relief treatment and artificial aging treatment. It is a commercially available material, and detail of the heat treatment conditions are unknown. The chemical composition and the mechanical properties of the material are shown in Table 1 and 2. The microstructure is shown Fig. 2. In this material, an oriented texture is well developed in the axial direction.

Table 1 Chemical composition of the material (%)

Si	Fe	Cu	Mn	Cr	Zn	Ti	Ti + Zr	Al
0.08	0.19	1.6	0.04	2.6	5.8	0.01	0.02	Bal

Table 2 Mechanical properties of the material (experimental data)

Tensile strength σ_B MPa	0.2% proof stress $\sigma_{0.2}$ MPa	Elongation δ %	Reduction of area Ψ %	Hardness Hv
685	631	12.6	23.4	189

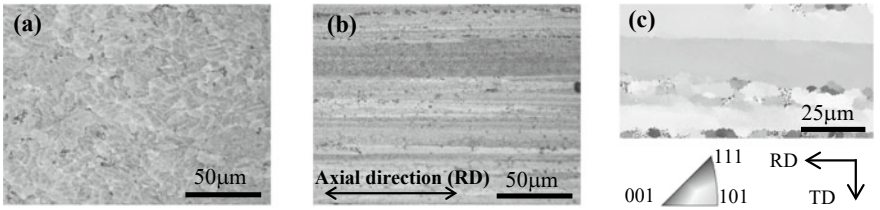

Fig. 2 Microstructure of material **a** cross section **b** longitudinal section **c** EBSD analysis result (IP Map)

2.2 Specimen and Fatigue Test

The shape of the test specimens in this study is shown in Fig. 3. The stress concentration factor of this shape is 1.074 [6]. The LP treatment was applied only to the notch area. The laser device used in this study was a prototype handheld pulse laser oscillator provided by OPTOQUEST Co., Ltd. The pulse width of this oscillator is 1.3 ns. An over-view of the laser peening system is shown in Fig. 4. The LP treatment was performed under the following conditions; an irradiation energy of 1.68 mJ, a spot diameter of 0.3 mm, a repetition rate of 50 Hz, and laser irradiation densities of 400 and 800 pulse/mm^2. The LP-treated specimen with under the condition of 400pulse/mm^2 is called 400pls, and the one with under the condition of 800pulse/mm^2 is called 800pls. Cantilever type rotating bending fatigue test was carried out with a rotating speed of 4000 rpm in the air at room temperature.

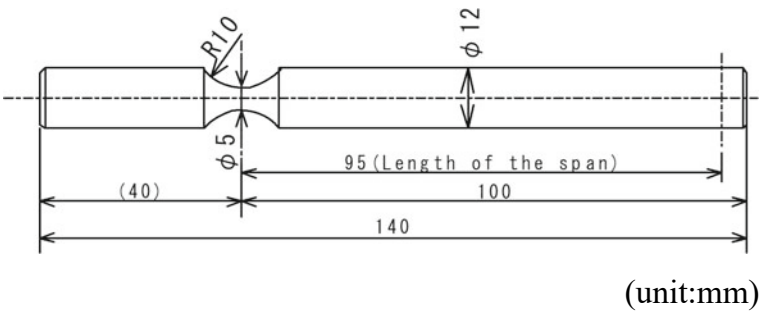

Fig. 3 The shape of fatigue test specimen

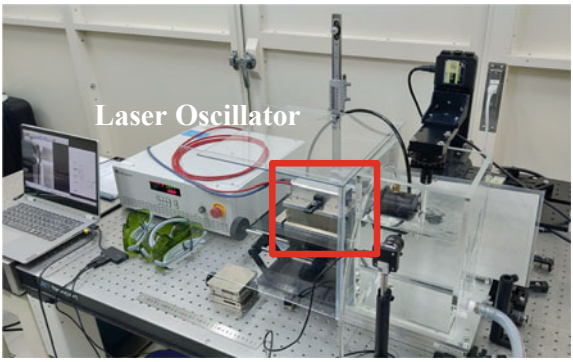

Fig. 4 Over-view of laser peening system

3 Experimental Results and Discussion

3.1 Fatigue Results

The S–N curves of the rotating bending fatigue testing result are shown in Fig. 5. The fatigue properties of A7075BE-T6511 were significantly improved by the handheld LP treatment. The difference in fatigue properties between 400 and 800pls was not significant. The handheld LP treatment improved the fatigue strength at 10^7 cycles by about 1.5 times and extended the fatigue life by about 100 times compared to those of the non-peened materials. These fatigue results indicate that the newly developed handheld pulse laser oscillator can be used for LP treatment. Typical fatigue fracture surface models are shown in Fig. 6. These surface modeling images were obtained from 3D models constructed by X-ray CT observations. There was a big difference between the non-peening specimens and the LP specimens. The fracture surfaces of all the non-peening specimens were on a flat plane perpendicular to the axial direction as shown in Fig. 6a. On the other hand, most of the fracture surfaces of the LP specimens have a slant part as shown in Fig. 6b, c. From the fracture surface observation results by optical microscope and scanning electron microscope, it was suggested that this slant part was not the final fracture site but the fatigue crack initiation site. The angle of the slant part to the cross section of the specimen was about 55–60°. From the results of crystal orientation analysis (EBSD analysis), it was clear that this material had an oriented texture in the axial direction in which the (001) plane of the fcc crystal structure coincides with the cross section of the specimen. The angle of the slant part agrees with 54.7 degrees which is the angle of the slip system $\{111\} < 110 >$ for the cross section of specimen.

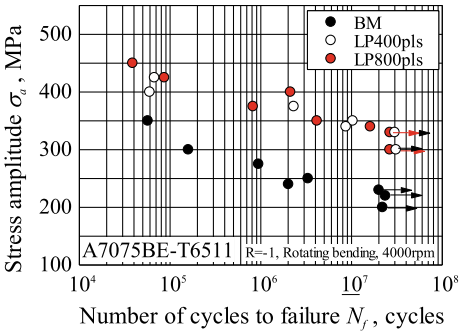

Fig. 5 S–N curves obtained by fatigue testin

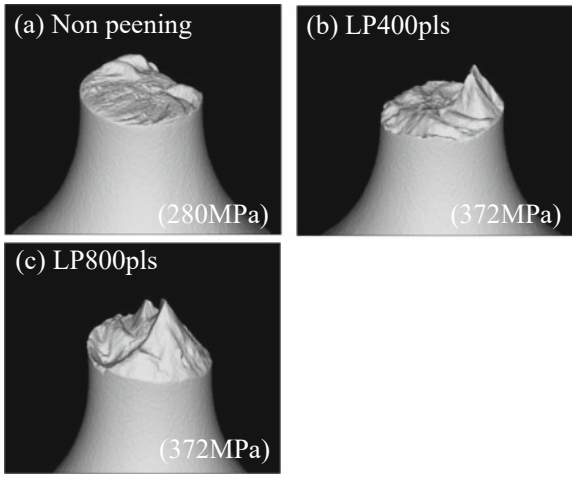

Fig. 6 Surface modeling images of fracture surfaces

3.2 Peening Effect and Fracture Mechanism

Hardness and residual stress, which were the main peening effects of fatigue property improvement, were investigated. The hardness distributions of the LP specimens are shown in Fig. 7. Strain hardening due to the handheld LP treatment is slight. Only the condition of LP800pls shows a slight increase in the surface hardness value. The thickness of the hardened layer is about 50 μm and the increase value is about 20Hv. The residual stress distributions of the LP specimens are shown in Fig. 8. The LP specimens have a large compressive residual stress near the surface layer despite a small increase in hardness. This phenomenon is one of the characteristics of handheld LP treatment. Although it is not clear from the hardness distribution, it is thought that the microstructure at only the specimen surface is in a significantly hardened state or in a highly strained state. It is considered that the generation and propagation of surface cracks are prevented by the high compressive residual stress and special surface state. The reason for the formation of this special surface state is thought to

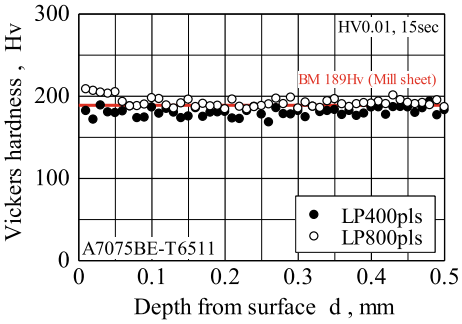

Fig. 7 Hardness distributions of LP specimens

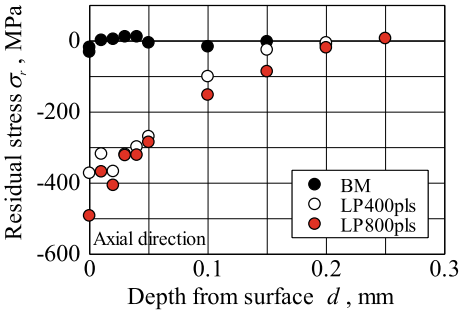

Fig. 8 Residual stress distributions of specimens

be related to the fact that the pulse width of the handheld pulse laser oscillator is less than 1/10 that of conventional pulse laser oscillators. We plan to investigate the details in the future. Even if the fatigue crack can be generated at the surface, the fatigue crack cannot grow in mode I, which is the crack open mode. More than that, the large-scale glide plane decohesion occurred inside the test specimen due to the influence of the developed texture in a triaxial stress state.

4 Conclusion

In order to investigate the effectiveness of the newly developed handheld pulse laser oscillator as a laser source of LP treatment, rotating bending high cycle fatigue tests were conducted on A7075BE-T6511 material used for aircraft components. The fatigue strength at 10^7 cycles is improved by about 1.5 times, and the fatigue life is extended by about 100 times than those of the non-peening material. It is clarified that the newly developed handheld pulse laser oscillator can be used for LP treatment and that it can be applied in a wide variety of industrial fields.

Acknowledgements This work was partially supported by the JST-MIRAI Program (grant number JPMJMI17A1), the Supporting Industry Program of the Small and Medium Enterprise Agency (grant number 202041907014), the Amada Foundation (grant number AF-2020239-C2), and the

Impulsing Paradigm Change through Disruptive Technologies Program (ImPACT) of the Council for Science, Technology and Innovation.

References

1. Sano Y, Mukai N, Okazaki K, Obata M (1997) Residual stress improvement in metal surface by underwater laser irradiation. Nucl Instrum Methods Phys Res B 121:432–436
2. Clauer AH (2019) Laser shock peening, the path to production. Metals 9:626
3. Sano Y (2020) Quarter century development of laser peening without coating. Metals 10:152
4. Sano Y, Kato T, Mizuta Y, Tamaki S, Yokofujita K, Taira T, Hosokai T, Sakino Y (2022) Development of a portable laser peening device and its effect on the fatigue properties of HT780 butt-welded joints. Forces in Mech 7:100080
5. Sano Y, Masaki K, Mizuta Y, Tamaki S, Hosokai T, Taira T (2021) Effects of laser peening with a pulse energy of 1.7 mJ on the residual stress and fatigue properties of A7075 aluminum alloy. Metals 11:1716
6. Walter DP, Deborah FP (2007) Third edition—Peterson's stress concentration factors. Wiley

Developing Domeless, Circular Vibratory Finishing for Aerospace Applications

Jeremy Weng Keong Ho, Kai Liang Tan, and Swee Hock Yeo

Abstract This paper proposed a vibrofinisher with a unique design—domeless, non-elevating and circular bowl vibrofinisher to be used for the aerospace industry. Compared to conventional circular dome vibrofinishers, this new setup could be more effective for material removal and surface roughness improvement than current industrial practices because of its better accessibility to annular geometries. There was limited literature to support this statement. In this paper, a model of a cuboid-body vibration system was proposed and a numerical analysis of this design with reference to past papers of standard design was conducted. The theoretical analysis showed a high potential for faster material removal rate due to an increase of 80.5% in the excitation force and excitation moment of up to 144.6%. Both displacement and rotational angle increased by 68% and 47% respectively, which suggests a higher amplitude. Using the theoretical results, the law of abrasive law and a roughness model was used to substantiate the effectiveness of the domeless bowl as a potential replacement to both the trough and dome bowl.

Keywords Mass finishing · Vibratory finishing · Aerospace

J. W. K. Ho (✉) · S. H. Yeo
Nanyang Technological University, 50 Nanyang Ave, Singapore 639798, Singapore
e-mail: jeremy-ho@artc.a-star.edu.sg

S. H. Yeo
e-mail: mshyeo@ntu.edu.sg

J. W. K. Ho · K. L. Tan
Advanced Remanufacturing & Technology Centre (ARTC), Agency for Science, Technology and Research (A*STAR), 3 CleanTech Loop, #01-01 CleanTech Two, Singapore 637143, Republic of Singapore
e-mail: tan_kai_liang@artc.a-star.edu.sg

N. Maharjan and W. He (eds.), *Proceedings of the 3rd International Conference on Advanced Surface Enhancement (INCASE) 2023*, Lecture Notes in Mechanical Engineering, https://doi.org/10.1007/978-981-99-8643-9_2

1 Introduction

Aerospace components, such as turbine blades, fans, vanes, stator rings, and blisk or integrally bladed rotors, play a critical role in aircraft engines, ensuring aerodynamic efficiency and service life. Surface integrity, both in terms of surface and sub-surface characteristics, is vital for their performance and safety. Vibratory finishing, a popular mass finishing process, is widely used in the aerospace industry due to its versatility in handling components of various sizes and meeting production schedules. Different machine variations and shapes, including domeless round vibrofinishers, are employed to target specific geometries and enhance the interaction between the media and the components. However, there is a lack of research on the application of domeless round vibrofinishers for annular aerospace components, warranting further investigation. This paper aims to conduct a theoretical study on a domeless, circular vibrofinisher and compare its performance to a conventional dome round vibrofinisher using numerical and economic analysis.

2 Theoretical Analysis Methodology

The domeless, circular vibratory finishing machine can be modelled using a spring-dampening-load dynamic system in x–y–z axes as seen in Fig. 1.

With reference to the model of the dome vibratory finishing machine by Hashimoto and Johnson [1], we can simplify the bowl as a charged cuboid-body with mass, M, representing the total mass which includes the mass of the bowl, media, component,

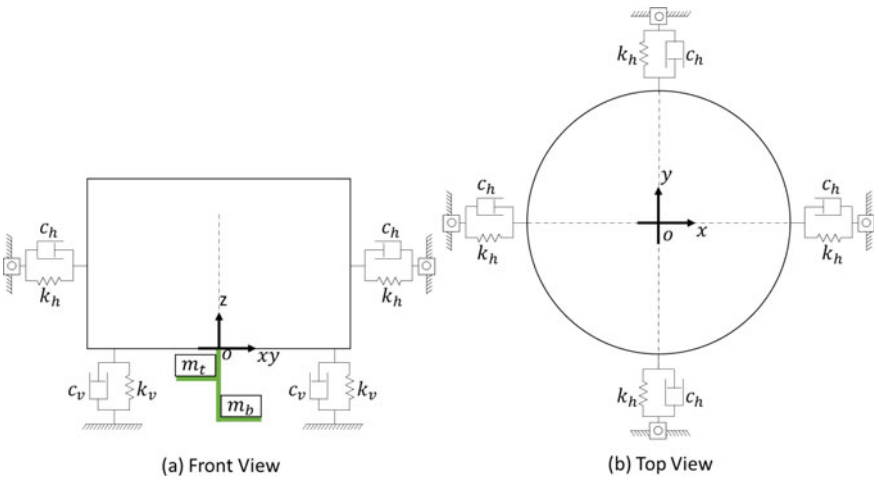

Fig. 1 Dynamic Model of domeless vibratory finishing bowl with indicative position of eccentric weights attached under the bowl

fixture, liquid compound, and water. This mass M is induced with forced vibration by two eccentric plates with attached flyweights along two ends of a motor shaft. The motor rotates and generates a centrifugal force to trigger the forced vibration. At the same time, a moment of inertia J is generated from the centrifugal force. The two eccentric plates are labelled top and bottom plates and are respectively labelled as mt, mb, with their rotational movement along the motor shaft as angular velocity, Ω. The alignment angle between the two masses will be labelled as the phase angle, φ. The distance from the centroid which is the motor axial shaft to the centroid of the flyweights is labelled as r.

Similar to Fig. 1, the springs supporting the mass, M, are consolidated into 4 spring/dampener at the corners on the body vertically (z-axis) while horizontally (x–y-axes) supported by 4 spring/dampener as well. To which the springs are labelled as kh and kv in the horizontal and vertical direction respectively, and dampeners labelled as ch and cv in the horizontal and vertical direction respectively as well.

The distance of the vertical springs from the centroid of M is labelled as L. Finally, mass M is understood to rotate along the x and y axes but not along the z axis. Therefore, there is a rotational angle along x and y axes, θx and θy respectively. The full representation is drawn in Fig. 2.

A set of parametric equations can be used to explain the model, as represented in Fig. 4 Schematic drawings of estimated positions and dimensions of Lt and Lb of (left) dome and (right) domeless Fig. 3. By using Newton's Second Law, the forces in a mechanical vibration system in the x–y-z coordinate can be established as follows:

$$F_x = M\ddot{x} + C_h\dot{x} + K_h x \tag{1}$$

$$F_y = M\ddot{y} + C_h\dot{y} + K_h y \tag{2}$$

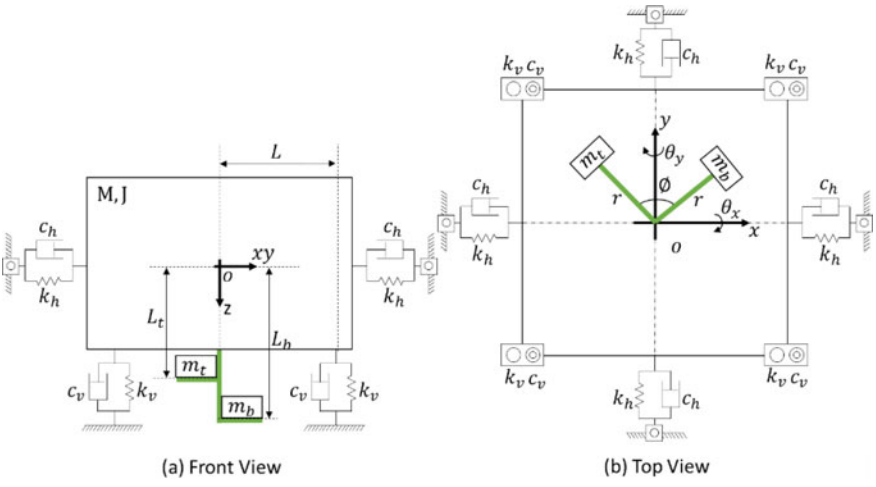

Fig. 2 Domeless vibratory finishing machine modelled as a mechanical vibration system

$$F_z = M\ddot{z} + C_h z + K_h z \tag{3}$$

With the nature of the bowl vibration, we can assume small values for θx and θy which approximated as $\sin\theta_x \approx \theta_x$, $\cos\theta_x \approx 1$, $\sin\theta_y \approx \theta_y$ and $\cos\theta_y \approx 1$. Therefore, F_z can be equated as:

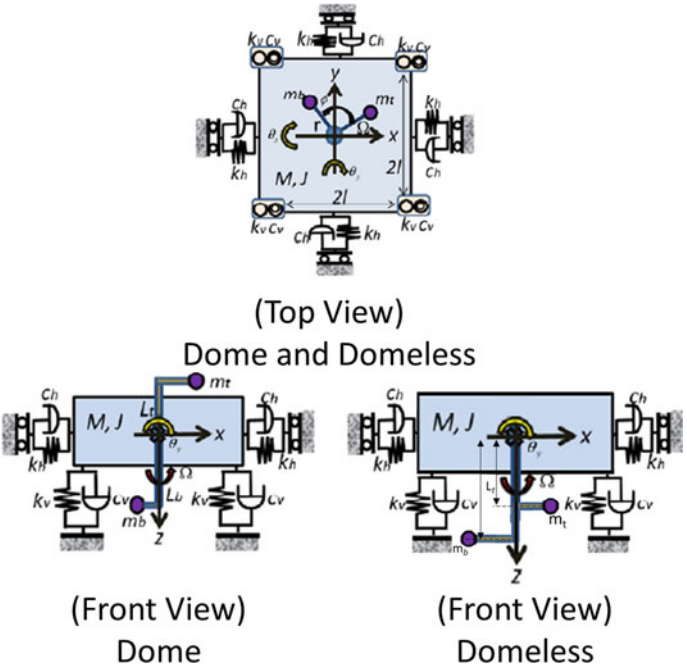

Fig. 3 Schematic drawing of dome and domeless, top view represented similar for both designs, while front view vary in terms of positioning of eccentric plates

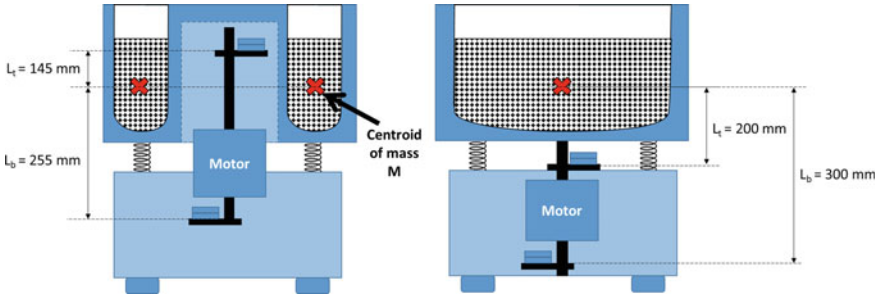

Fig. 4 Schematic drawings of estimated positions and dimensions of L_t and L_b of (left) dome and (right) domeless

$$F_z = F_x\theta_x + F_y\theta_y \tag{4}$$

The angular motion equations are established as follows:

$$P_X = J\ddot{\theta}_x + \left(C_v L^2\right)\dot{\theta}_x + \left(K_v L^2\right)\theta_x \tag{5}$$

$$P_y = J\ddot{\theta}_y + \left(C_v L^2\right)\dot{\theta}_y + \left(K_v L^2\right)\theta_y \tag{6}$$

$$P_z = J\ddot{\theta}_z = 0 \tag{7}$$

where $C_v = 4\,c_v$, $K_v = 4k_v$, $C_h = 2c_h$, $K_h = 2k_h$.

Using Fig. 2 to establish the dynamic positioning of top and bottom eccentric masses mt and mb during processing, we can establish the linear and rotational forces along x–y axes as:

$$F_x = r\Omega^2[m_t \cos\Omega t + m_b \cos(\Omega t + \varphi)] \tag{8}$$

$$F_y = r\Omega^2[m_t \sin\Omega t + m_b \sin(\Omega t + \varphi)] \tag{9}$$

$$P_X = r\Omega^2[m_t L_t \sin\Omega t + m_b L_b \sin(\Omega t + \varphi)] \tag{10}$$

$$P_y = r\Omega^2[m_t L_t \cos\Omega t + m_b L_b \cos(\Omega t + \varphi)] \tag{11}$$

Finally, the motion Eqs. (1)–(3), (5) and (6) can be solved to yield free and forced vibrations. A general solution of the second order differential equation of each of the Eqs. (1)–(3), (5) and (6) can be summated by the auxiliary solution with subscript c to label the free vibrations equations and particular solution subscript p to label the forced vibration equations. This is to follow the model of Hashimoto and Johnson [1] to enable comparison in the next chapter. Therefore, $x = x_c + x_p$, $y = y_c + y_p$, $z = z_c + z_p$, $\theta_x = \theta_{xc} + \theta_{xp}$ and $\theta_y = \theta_{yc} + \theta_{yp}$.

It is also noted that is a slight variation to Eqs. (10) and (11) for a domeless-type due to the change in direction of L_t as compared to a dome-type. Hence, the free vibrations in the x–y–z coordinates and their rotational axes, with the exception of rotation along z axis, are represented by the following equations:

$$\mathrm{x_c} = \mathrm{A_1 e^{-\zeta_h \omega_{nh} t}} \sin(\omega_{dh} t - \psi_1) \tag{12}$$

$$\mathrm{y_c} = \mathrm{A_2 e^{-\zeta_h \omega_{nh} t}} \sin(\omega_{dh} t - \psi_2) \tag{13}$$

$$\mathrm{z_c} = \mathrm{A_3 e^{-\zeta_v \omega_{nh} t}} \sin(\omega_{dv} t - \psi_3) \tag{14}$$

$$\theta_{xc} = A_4 e^{-\zeta_h \omega_{nh} t} \sin(\omega_{dh} t - \psi_4) \tag{15}$$

$$\theta_{yc} = A_5 e^{-\zeta_h \omega_{nh} t} \sin(\omega_{dh} t - \psi_5) \tag{16}$$

where A1—A5 are arbitrary constants, ψ_1 to ψ_5 are alignment (phase) angles determined by arbitrary constants. ζ represents the damping factors, ωn represents natural frequency and ωd represent damped natural frequency, with all three having subscripts to represent their directions—v for vertical, h for horizontal and θ for rotational. Each of them can be calculated with the following equations:

$$\zeta_h = \frac{C_h}{2\sqrt{MK_h}} \tag{17}$$

$$\omega_{nh} = \sqrt{\frac{K_h}{M}} \tag{18}$$

$$\omega_{dh} = \left(\sqrt{1 - \zeta_h^2}\right)\omega_{nh} \tag{19}$$

$$\zeta_v = \frac{C_v}{2\sqrt{MK_v}} \tag{20}$$

$$\omega_{nh} = \sqrt{\frac{K_v}{M}} \tag{21}$$

$$\omega_{dv} = \left(\sqrt{1 - \zeta_v^2}\right)\omega_{nv} \tag{22}$$

$$\zeta_\theta = \frac{C_v L}{2\sqrt{MK_v}} \tag{23}$$

$$\omega_{n\theta} = \sqrt{\frac{K_v L^2}{J}} \tag{24}$$

$$\omega_{d\theta} = \left(\sqrt{1 - \zeta_\theta^2}\right)\omega_{n\theta} \tag{25}$$

The forced vibrations generated by the rotational angular velocity Ω of eccentric masses mt and mb are represented by the auxiliary equations of Eqs. (1)–(5) in the x–y-z coordinates and their rotational axes, with the exception of rotation along z axis, by the following equations:

$$x_p = G_x \cos(\Omega t - \Phi_1) \tag{26}$$

$$y_p = G_y \sin(\Omega t - \Phi_1) \tag{27}$$

$$z_p = constant \tag{28}$$

$$\theta_{xp} = E_x \sin(\Omega t - \Phi_2) \tag{29}$$

$$\theta_{yp} = E_y \cos(\Omega t - \Phi_2) \tag{30}$$

where Φ is the alignment or phase angle and variables G, E are variables, with their subscripts to represent their directional axis, are determined by the following equations:

$$G_x = \frac{F_x}{\sqrt{(C_h\Omega)^2 + (K_h - M\Omega)^2)^2}} \tag{31}$$

$$G_y = \frac{F_y}{\sqrt{(C_h\Omega)^2 + (K_h - M\Omega)^2)^2}} \tag{32}$$

$$E_x = \frac{P_x}{\sqrt{(C_v L^2\Omega)^2 + (K_v L^2 - J\Omega)^2)^2}} \tag{33}$$

$$E_y = \frac{P_y}{\sqrt{(C_v L^2\Omega)^2 + (K_v L^2 - J\Omega)^2)^2}} \tag{34}$$

$$\Phi_1 = \tan^{-1} \frac{C_h\Omega}{(K_h - M\Omega^2)} \tag{35}$$

$$\Phi_2 = \tan^{-1} \frac{C_h L^2\Omega}{(K_h L^2 - J\Omega^2)} \tag{36}$$

The Eqs. (1)–(36) will be used as reference with Hashimoto and Johnson's [1] dome model to be described and comparatively plotted.

2.1 Comparison to Dome, Circular Vibratory Finishing

According to Hashimoto and Johnson's mechanical vibration model [1], the domeless machine can be drawn as another re-representation from Fig. 2 to create a direct comparison of between a dome and domeless schematic as shown in Fig. 3.

The key different difference between a dome and domeless vibratory finishing machine is the position of the eccentric plates. Parameters are taken from the paper from Hashimoto and Johnson [1] and scaled accordingly to have a fair comparison between dome and domeless type. A parameter table is established in Table 1.

Table 1 Parameters to be used for comparison

Parameter	Symbol	Dome	Domeless
Phase angle (alignment angle between eccentric plates)	φ	$90° \approx 1.5708$ rad/s	
Angular velocity	Ω	146.9 rad/s	
Spring constant—vertical	k_v	39.2 N/mm	
Spring constant—horizontal	k_h	15.9 N/mm	
Damping constant—vertical	c_v	0.0055 N s/mm	
Damping constant—horizontal	c_h	0.0222 N s/mm	
Damping factors—vertical	ζ_v	0.0031	
Damping factors—horizontal	ζ_h	0.0014	
Damping factors—angular	ζ_θ	0.0031	
Natural frequency—vertical	ω_{nv}	44.6 rad/s	
Natural frequency—horizontal	ω_{nh}	20.1 rad/s	
Natural frequency—angular	$\omega_{n\theta}$	45.1 rad/s	
Damping frequency—horizontal	ω_{dv}	44.6 rad/s	
Damping frequency—vertical	ω_{dh}	20.1 rad/s	
Damping frequency—angular	$\omega_{d\theta}$	45.1 rad/s	
Horizontal length of vertical springs to mass M centroid	L	180 mm	
Horizontal length of eccentric plate to mass M centroid	r	50 mm	
Vertical length of top eccentric plate to mass M centroid	L_t	145 mm	200 mm
Vertical length of bottom eccentric plate to mass M centroid	L_b	255 mm	300 mm
Top eccentric plate and flyweight (pre-assigned) weight	$m_t \cdot g$	8.4 N	8.4 N (2 plates*)
Bottom eccentric plate and flyweight (pre-assigned) weight	$m_b \cdot g$	9.3 N	21.0 N (5 plates*)
Ratio of top eccentric plate and flyweight and bottom eccentric plate and flyweight	m_t / m_b	1 (round up)	0.4
Body weight	$M \cdot g$	772.3 N	816.1 N

*Based on weight referred from study Hashimoto & Johnson [1] and industrial practice for top/bottom flyweights' setup to be 2:5

To ensure a proper baseline comparison, machine setups that are similar in nature for both types such as springs, and dampeners will be kept constant. The process setup such as alignment (phase) angle and angular velocity will also be set similar. Additionally, natural constants and factors will be set similar. Therefore, the similar values are as follows: φ, Ω, k_v, k_h, c_v, c_h, ζ_h, ζ_v, ζ_θ, ω_{nh}, ω_{nv}, $\omega_{n\theta}$, ω_{dh}, ω_{dv}, $\omega_{d\theta}$, L, and r.

The key difference between the two bowl types will be on the masses and their relative locations. For eccentric masses m_t and m_b, a baseline qualitative ratio of m_t and m_b was used depending on the number of flyweights are attached to them.

Additionally, the flyweight quantity will be selected based on the dome and domeless current best practice to achieve an equal frequency and amplitude. This is done by using reference of ERBA EVP-250 dome and ERBA EVP-250 CL domeless equipment. For a similar setup between dome and domeless-type, a 4.5 mm amplitude and 70° lead angle for the feed frequency will require to have two flyweight at the top and bottom plates respectively for a dome-type. This makes the ratio of m_t/m_b 1:1. In a domeless-type setup, it is two at the top and five at the bottom, making the ratio 2:5. To summarise, the values of 1.0 for dome and 0.4 for domeless is used.

The difference between dome and domeless types for positions L_t and L_b are mainly that direction of L_t is under the bowl and therefore opposite in direction as opposed to dome type, and that L_b is further from the centroid M as compared to dome type due to the lowered placement of the motor. These observations of domeless type with comparison were based on the difference in EVP-250 CL domeless and EVP-250 dome type machines, respectively. Based on these pointers, for domeless type eccentric weight positions, L_t and L_b, will be estimated based on the study's machine specification [1] and also with industrial best practices, are placed at the values 200 mm and 300 mm as drawn in Fig. 4.

For body mass M of dome machine will be calculated based on similar media (Al_2O_3 spherical dia. 5 mm) of density 1.43 g/cm^3 and component mass (hardened steel cylindrical roller of dia. 15 mm x L22 mm, HRC62) from the paper. As the mass M of dome type will account for the additional volume due to the lack of a dome by a calculated approximation of 3.123L, which is the volume of the dome. Using this additional volume to calculate the weight from the additional media, the weight of the bowl (assume weight is similar for domeless-type as dome is hollow therefore weight is negligible), and weight of the component, will amount 816.1 N. The detailed calculations are appended in Appendix A.

3 Theoretical Comparison Results

Figure 5 show a comparison of dome and domeless type of the external forces in x and y axes, which are the sources of the vibration motion during machine operation with an amplitude of 1400 RPM. This is calculated by Eqs. (8) and (9). The results show that the domeless type has its excitation force amplitude peak higher than dome type at 2.44 kN, compared to domeless type at 1.352 kN, a difference of around 80.5%.

Figure 6 shows a comparison of dome and domeless type of the external moments in x and y axes. This is calculated by Eqs. (8) and (9) for domeless type and cited from the study for dome type [1]. The results show that the domeless type has its excitation moment amplitude peak higher than dome type at 703.5kN, compared to domeless type at 287.7kN, a difference of 144.6%. It is also noted that there is a shift in frequency by almost 50%.

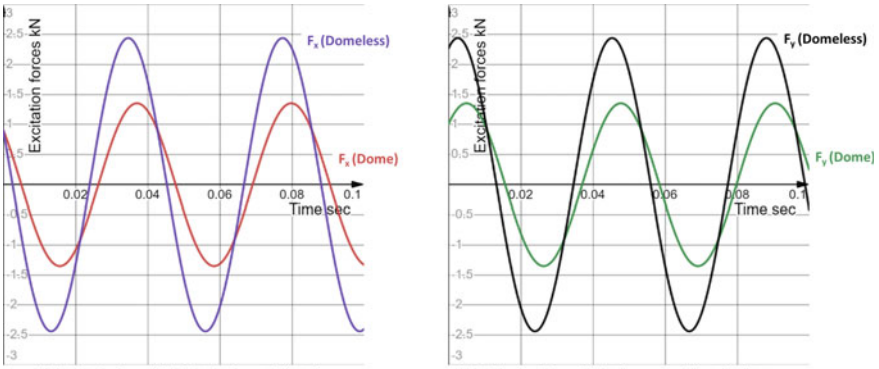

Fig. 5 Theoretical comparison between dome and domeless-type by the external forces causing the forced vibration in **a** horizontal and **b** vertical direction

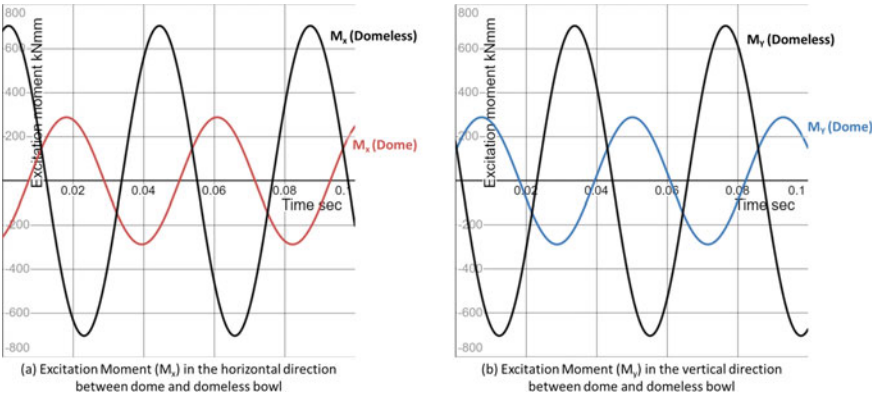

Fig. 6 Theoretical comparison between dome and domeless-type by the external moment causing the forced vibration in rotational directions in horizontal axes along **a** X-axis and **b** Y-axis

4 Discussion

Based on results shown in Figs. 5 and 6, there is an agreement to qualitative reasoning of a higher processing capability. With the absence of the dome, there is a larger radial roll which allow longer displacement of component-media contact. This in turn provides a longer exposure for material removal. To validate this statement, the law of abrasive wear [2] can be used:

$$V_s = \frac{k_s N L}{H} \tag{37}$$

V_s wear volume

k_s wear coefficient
N normal load
H hardness of worn surface
L media sliding distance

In this equation, the normal load (N) is the perpendicular force acting on the component surface and thus is directly proportionate to the wear volume (V_s). From an energy standpoint, the larger radial roll caused by an increased excitation forces from the bowl vibration will cause an increased energy transfer from the bowl vibration to media and finally onto the component surface. Hence, this implies a higher material removal due to higher excitation forces from the bowl.

Illustrated in Fig. 7, a micro view of a component-media contact point can be used to show a conversion of the law of abrasive wear into a steady-state abrasive wear per unit area. Thus, wear volume (V_s) is converted into wear depth per unit time, $\delta h_s \delta t$ and normal load (N) is converted into normal specific load (p_g) per unit area, $p_g \delta A$. This allows a roughness model to be derived as done by Wan et al. [3]):

$$R_a = (R_i - R_E) \cdot e^{-\frac{k_T p_g v_s}{H} t} + R_E \tag{38}$$

R_a Current Roughness
R_E Roughness at saturation
R_i Initial Roughness
v_s Velocity along unit area
k_T wear coefficient

By making time (t) the subject:

$$\mathrm{t} = \frac{-\mathrm{H} \cdot \ln\left(\frac{R_a - R_E}{R_i - R_E}\right)}{k_T p_g v_s} \tag{39}$$

The Eq. (39) shows that the normal specific load (p_g) is inversely proportionate to time (t). As earlier described, the higher excitation forces caused by a domeless-type as compared to a dome-type will cause an increase in energy transfer from the

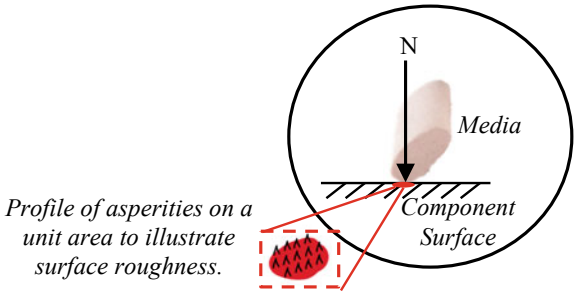

Fig. 7 Illustration of media contact to component surface with a micro illustration of surface roughness per unit area

bowl to component-media interaction via the point contact. This point contact is referred as the normal specific load (p_g), which essentially proves that time taken for surface finishing will reduce. Hence, a potentially faster surface finishing by using domeless-type.

5 Conclusion

This paper proposed a new vibratory finishing machine with a unique design—domeless, non-elevating and circular vibratory finishing bowl—to be used for the aerospace industry. A study on current industrial best practices such as machine-component pairing was conducted, and it was determined that this proposed machine could be more effective than current industrial practices.

A review of existing vibratory finishing models was conducted, and a model of a cuboid-body vibration system was adapted. Through a theoretical comparison with a dome-type, the domeless-type showed a higher processing potential than dome type vibratory finishing due to the increase in excitation forces by 80.5%. Additionally, the increased distance between the motor and two eccentric plates to the centroid of the bowl mass augmented the forced vibration component of the bowl and increased the excitation moment by up to 144.6%. This suggests that a domeless-type allows a larger roll radius due to the absence of the dome. The displacement value showed an increase of 68% and rotational angle increase of 47%. This suggests that a domeless-type could result in a higher bowl amplitude. Overall, these results showed higher processing potential and were substantiated through an inference to the law of abrasive wear and a roughness model by Wan et al. [3].

References

1. Hashimoto F, Johnson S (2015) Modeling of vibratory finishing machines. CIRP Ann Manuf Technol 64:345–348
2. Hutchings IM (1992) Tribology: friction and wear of engineering.Materials, London
3. Wan S, Liu Y, Woon K (2016) A simple general process model for vibratory finishing. Int J Adv Manuf Technol 86:2393–2400